Advanced Functional Materials

ADVANCED FUNCTIONAL MATERIALS
www.afm-journal.de

RESEARCH ARTICLE

Nanoscale Local Symmetry Optimization Induced Low Lattice Thermal Conductivity in I-V-VI$_2$ Compounds

Changyuan Li[1] | Di Zhang[1] | Xiaoyu Zhang[1] | Hongyao Zhang[2] | Jiang Cheng[3] | Zhiwei Chen[1] | He Lin[2] | Xiang Meng[3] | Wen Li[1] | Long Yang[1]

[1]Interdisciplinary Materials Research Center, School of Materials Science and Engineering, Tongji University, Shanghai, China | [2]Shanghai Advanced Research Institute, Chinese Academy of Sciences, Shanghai, China | [3]School of Materials Science and Engineering, Chongqing University of Arts and Sciences, Chongqing, China

Correspondence: Xiang Meng (xiang.meng@hotmail.com) | Wen Li (liwen@tongji.edu.cn) | Long Yang (long_yang@tongji.edu.cn)

Received: 3 December 2025 | **Revised:** 12 February 2026 | **Accepted:** 23 February 2026

Keywords: lattice thermal conductivity | local structure optimization | pair distribution function | thermoelectrics

ABSTRACT

The intrinsically low lattice thermal conductivity (κ_L) caused by lone pair electrons makes I-V-VI$_2$ compounds promising candidates for thermoelectric applications. Elucidating the underlying mechanism of the correlation between lone pair electrons and defects plays an important role in providing critical insights for further designing low κ_L materials. This work employs X-ray pair distribution function analysis to probe the nanoscale local atomic structures of I-V-VI$_2$ compounds, using AgSbSe$_2$ as the model material to understand the structure-property relationship. The stereochemically active lone pair electrons on Sb^{3+} induce significant off-centering displacements, introducing local symmetry breaking that can be systematically tuned through controlled vacancies, atomic disordering, or substitution. Theoretical calculations validate the connection between structural distortions and chemical bonding strength, resulting in the change of κ_L. This work not only unveils the local structure evolution of AgSbSe$_2$ during alloying, but also provides a roadmap for performance optimization of I-V-VI$_2$ compounds with lone pair electron effects.

1 | Introduction

The thermoelectric materials can realize the direct conversion between heat and electricity, providing a novel approach to solving environmental issues. The conversion efficiency is determined by the dimensionless figure of merit zT, $zT = S^2 T/\rho(\kappa_E + \kappa_L)$, where S, T, ρ, κ_E, and κ_L represent the Seebeck coefficient, the absolute temperature, electrical resistivity, and electronic and lattice thermal conductivity, respectively. Due to the strong coupling correlation between S, ρ, and κ_E, the lattice thermal conductivity (κ_L), as the only independently adjustable parameter, has received extensive attention [1–3]. Effective strategies, such as defect engineering for reducing κ_L have been widely studied in recent years [4–6]. The materials with complex crystal structures [7] and strong anharmonicity [8] will exhibit intrinsically low κ_L, which can be promising candidates for further optimizing κ_L to achieve excellent thermoelectric performance.

Ternary I-V-VI$_2$ compounds (I = Ag, Cu; V = Sb, Bi; and VI = S, Se, Te) have gained widespread research interest due to their intrinsically low κ_L [9]. Some Ag-based I-V-VI$_2$ compounds, such as AgInSe$_2$ and AgGaTe$_2$, have been reported to exhibit intrinsically low lattice thermal conductivity due to the off-centering of Ag atoms [10–12]. By alloying with other systems, such as V-VI, the lattice thermal conductivity of I-V-VI$_2$ can be further optimized to obtain better thermoelectric performance [13, 14]. However, some researchers have reported an unconventional κ_L change in the I-V-VI$_2$ solid solution systems [15], which was recognized as the contribution from the lone pair electrons of the group V element in the local structure [9]. The pristine nanoscale local structural distortion induced by lone pair electron effects may significantly enhance the lattice anharmonicity and thus achieve intrinsically low κ_L [16, 17], and its relationship with introduced defects would be the key to optimizing κ_L in I-V-VI$_2$ solid solution systems.

The lone pair electron effects, as a significant structural origin for local distortions, have raised wide interest in the thermoelectric material field [9]. In pristine $AgSbSe_2$, the local distortion induced by lone pair electrons was investigated [18], revealing that the temperature-independent cationic off-centering significantly enhances lattice anharmonicity, leading to the glass-like thermal conduction. The substitution of a group V element has been reported to weaken the lone pair electron effects and increase κ_L in the $AgSbSnSe_3$ high-entropy system [19]. The element doping has been reported to manipulate the short-range ordering successfully to significantly reduce the total carrier scattering potential in $AgSbSe_2$ [20–22]. Substitution and doping have been successfully employed to optimize the thermal conductivity by introducing lone-pair electron effects, as demonstrated in $AgInSe_2$ [23] and $CuFeS_2$ [24], highlighting the potential of lone-pair-electron elements in doping engineering. Additionally, the lone pair electron effects are important for uncovering the thermal behaviors in many other material systems, such as TlSe-type compounds [25, 26], layered materials [27], and perovskites [28, 29]. The local structure manipulation, such as introducing defects into materials, would not only produce the long-range fluctuation of mass and strain, but also generate nanoscale lattice distortion to affect the phonon scattering mechanism. The introduced defects and the variation of lone pair electron effects can also significantly enhance the bonding inhomogeneity, leading to the low κ_L observed in a number of compounds [30–35]. Therefore, it is worthwhile to investigate the correlations between lone pair electron effects and defects on κ_L. A systematic study on local structural variation with defects would help achieve promising thermal performance in the I-V-VI$_2$ solid solution systems.

In this work, we employ $AgSbSe_2$ as an I-V-VI$_2$ model material with lone pair electrons to investigate the local structure evolution during alloying. The local structure manipulation of $AgSbSe_2$ was achieved by alloying with Sb_2Te_3. Owing to the non-equiatomic anion-to-cation ratio, the cation vacancy and anionic disorder were introduced into the system, where the former influences the local distortion of neighboring octahedra, while the anionic disorder changes the octahedral connectivity at shared vertices. Correspondingly, the local structure, which was studied by the pair distribution function (PDF) technique, gradually evolved to higher symmetry with more alloying. The theoretical calculation reveals that the introduced vacancies would reduce the local distortion, and the sound velocity change is attributed to chemical bonding strength variation, which results in the change of κ_L. The local-structure-oriented manipulation strategy is further validated by Cd substitution at the Sb^{3+} site, which demonstrates that reducing the concentration of Sb-centered octahedra lowers the lattice thermal conductivity. Furthermore, a newly developed 3D diffuse scattering technique was carried out against $AgSbSe_2$ single crystals, which is capable of collecting the diffuse scattering over the full 3D reciprocal space [36–39]. The significant diffuse scattering was observed in the pristine $AgSbSe_2$ single crystal, which represent the local structure deviations from the cubic averaged structure of $AgSbSe_2$ phase. This study provides an insight into the nanoscale local symmetry evolution through experimental and theoretical methods, and it offers practical guidance for local structure manipulation by lone pair effects for thermoelectric applications in the I-V-VI$_2$ system.

2 | Results and Discussion

The pristine $AgSbSe_2$ has a rock-salt cubic structure with a space group of $Fm\bar{3}m$, as shown in Figure 1a, where silver and antimony randomly occupy the cation site, and selenium occupies the anion position, forming the octahedra framework [40]. The atomic structure can be affected by the stereochemical activity of lone pair electrons on the Sb^{3+} site, thus inducing low κ_L, as reported in the literature [21, 41, 42]. In order to further optimize the κ_L, an alloying composition of $AgSbSe_2$ with non-equiatomic ratio Sb_2Te_3 was synthesized to manipulate local structures by cationic vacancy and anionic disordering. With the increasing Sb_2Te_3 alloying fraction, X-ray diffraction (XRD) results show that the average structure of $AgSb_{1+2x}Se_2Te_{3x}$ agrees well with the reported $AgSbSe_2$ crystalline structure (Figure 1b). Meanwhile, the diffraction peaks shifted to lower angles due to the lattice distortion induced by the larger ionic radius of the incorporated Te^{2-} (221 pm) [43] and atomic disorder within the anionic sublattice, resulting in the lattice expansion, which was consistent with the theoretical calculations (Figure S2). Some impurity peaks were observed for the sample with $x = 0.33$, suggesting the solid solubility of ~30% for Sb_2Te_3 in $AgSbSe_2$. The scanning electron microscopy (SEM) observation and energy-dispersive X-ray spectroscopy (EDS) analysis further validated the phase purity, as shown in Figure S3. The Hall measurement results show that the Seebeck coefficient decreases with the increase of carrier concentration during alloying (Figure S4a), and the scattering mechanism of charge carriers does not change significantly during alloying (Figure S4b).

To study the average structure of solid solutions quantitatively, the Rietveld refinement was carried out by GSAS-II software [44], which confirmed the cubic structure for all samples. The impurity peaks were identified to be Sb_2Te_3, and the proportion of impurity phase is about 3.7% in the $x = 0.33$ sample. The lattice parameters obtained from Rietveld refinements are shown in Figure 1c, which increase with the alloying fraction of Sb_2Te_3. However, the κ_L (Figure 1d) does not monotonically decrease with the alloying fraction. The κ_L decreases first for $x = 0 - 0.2$, but when more Sb_2Te_3 is incorporated, it starts to increase, even though the long-range structural symmetry remains unchanged. As shown in Figure S4c, d, despite changes in carrier concentration during alloying, the contribution of electronic thermal conductivity to the total thermal conductivity was estimated to be relatively small. The total thermal conductivity is dominated by the lattice thermal conductivity. Therefore, it is necessary to study the local structure evolution during alloying in more detail and to explore the interaction between introduced defects and pristine lone pair electron effects on lattice thermal conductivity.

The synchrotron X-ray PDF analysis has been carried out to study the local structure evolution systematically during alloying. As a

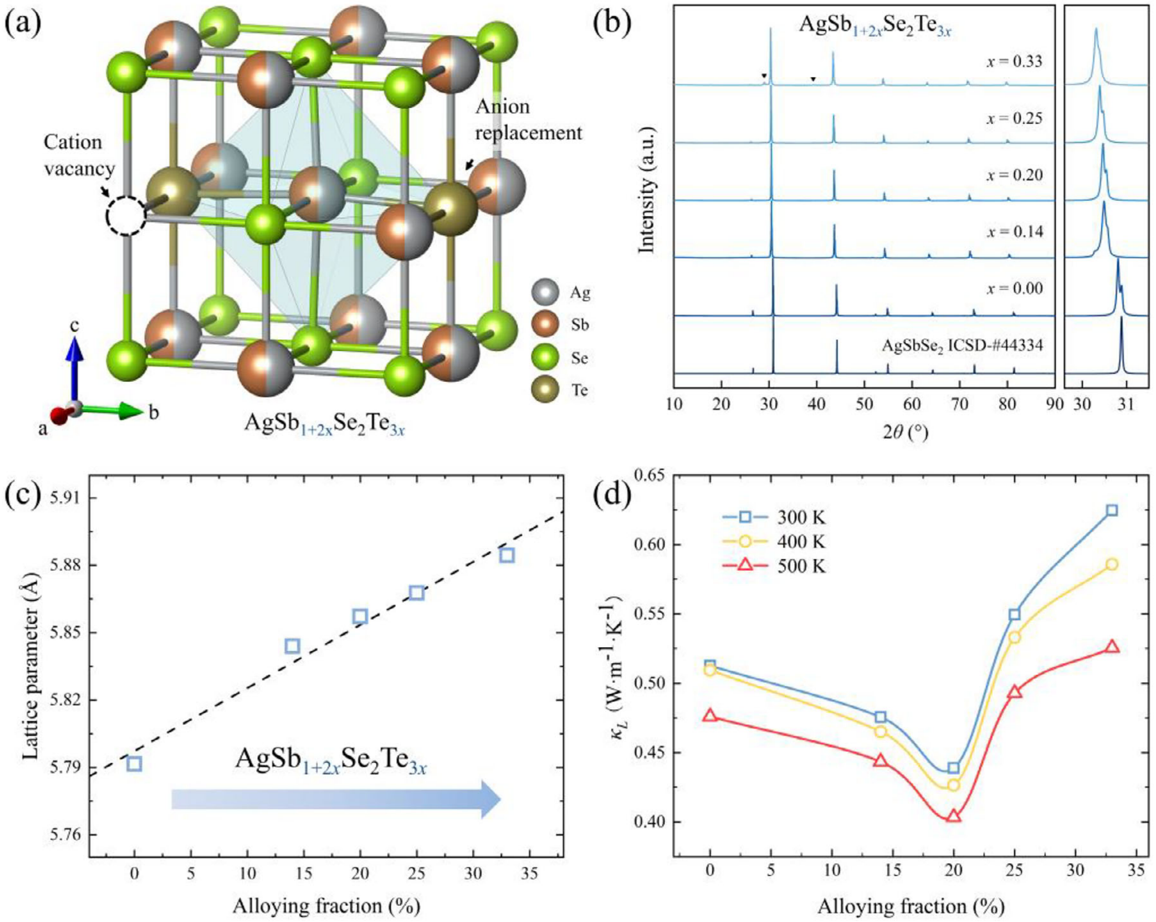

FIGURE 1 | (a) The cubic structure (space group: $Fm\bar{3}m$) of AgSb$_{1+2x}$Se$_2$Te$_{3x}$. Ag, Sb, Se, and Te atoms are represented by gray, orange, green, and brown, respectively. (b) Room-temperature powder XRD patterns of AgSb$_{1+2x}$Se$_2$Te$_{3x}$ ($0.0 \leq x \leq 0.33$). The impurity peak was marked in black triangles in AgSb$_{1.66}$Se$_2$Te ($x = 0.33$). Detailed information on Rietveld refinements can be found in Figure S1 and Table S1. (c) Room-temperature lattice parameters of AgSb$_{1+2x}$Se$_2$Te$_{3x}$ ($0.0 \leq x \leq 0.33$) obtained from Rietveld refinements of XRD data. (d) The experimental lattice thermal conductivities at 300, 400, and 500 K of AgSb$_{1+2x}$Se$_2$Te$_{3x}$ ($0.0 \leq x \leq 0.33$).

local structure probe, atomic PDF gives the short-range structural ordering in the real space directly [45, 46]. The PDF experiments were performed at BL12SW of Shanghai Synchrotron Radiation Facility [47] using the rapid acquisition PDF method (RAPDF) [48]. The pyFAI and PDFgetX3 programs were used for PDF data processing [49, 50], and the PDF modeling program PDFgui was used for structure refinements [51]. More detailed information can be found in the Supporting Information. Figure 2a shows the PDF structural refinement of long-range structure in pristine AgSbSe$_2$, which is in good agreement with $Fm\bar{3}m$ cubic structure model [40]. However, a significant misfit was observed in the local region (marked in blue). To better investigate the local structure environment, the first PDF peak is refined by the cubic structure of AgSbSe$_2$. As shown in Figure 2b (left), the first experimental peak position is found to be smaller than that of the cubic symmetry, and interestingly, a peak shoulder at 2.8 Å is observed. The peak position of PDF data represents the interatomic distance distribution, i.e., the atomic pair distance r in the material. For AgSbSe$_2$, the first PDF peak represents the nearest neighboring anion-cation bond length. For the case of averaged cubic structure, only one symmetric peak is allowed by the symmetry, which is contributed by six equal bond lengths from the regular (Ag,Sb)Se$_6$ octahedra (red curve in Figure 2b (left)). The asymmetric first peak in PDF data represents the pristine local structural distortion of AgSbSe$_2$, which indicates that the local structure environment deviates from the high-symmetry lattice site. As reported by previous studies [18, 19], the off-centering of cation position was attributed to the electronic configuration of Sb^{3+}, which has a pair of lone pair electrons in the 5s^2 orbital. The stereochemical activity of lone pair electrons in the local structure makes the neighboring atoms deviate from the average crystallographic position, thus resulting in three longer bonds and three shorter bonds in the (Ag,Sb)Se$_6$ octahedra, which is represented by the experimental PDF peak split ($r \sim 2.8$ Å). Therefore, distorted structural models with the off-center cation along the cubic [100], [110], and [111] directions were built to describe the local structural environment. For the low-r range of 2.0 to 4.6 Å, as in Figure 2b (right) and Figure S5, the cubic [111] distorted model results in better fit quality than other models, revealing the existence of distorted octahedra along cubic [111] direction in the local structure.

For solid solution compounds, the overall PDF structural refinement results are in good agreement with $Fm\bar{3}m$ cubic structure (Figure S6), and the variation trend of lattice parameters (Figure 2c) is also consistent with the XRD results. A similar

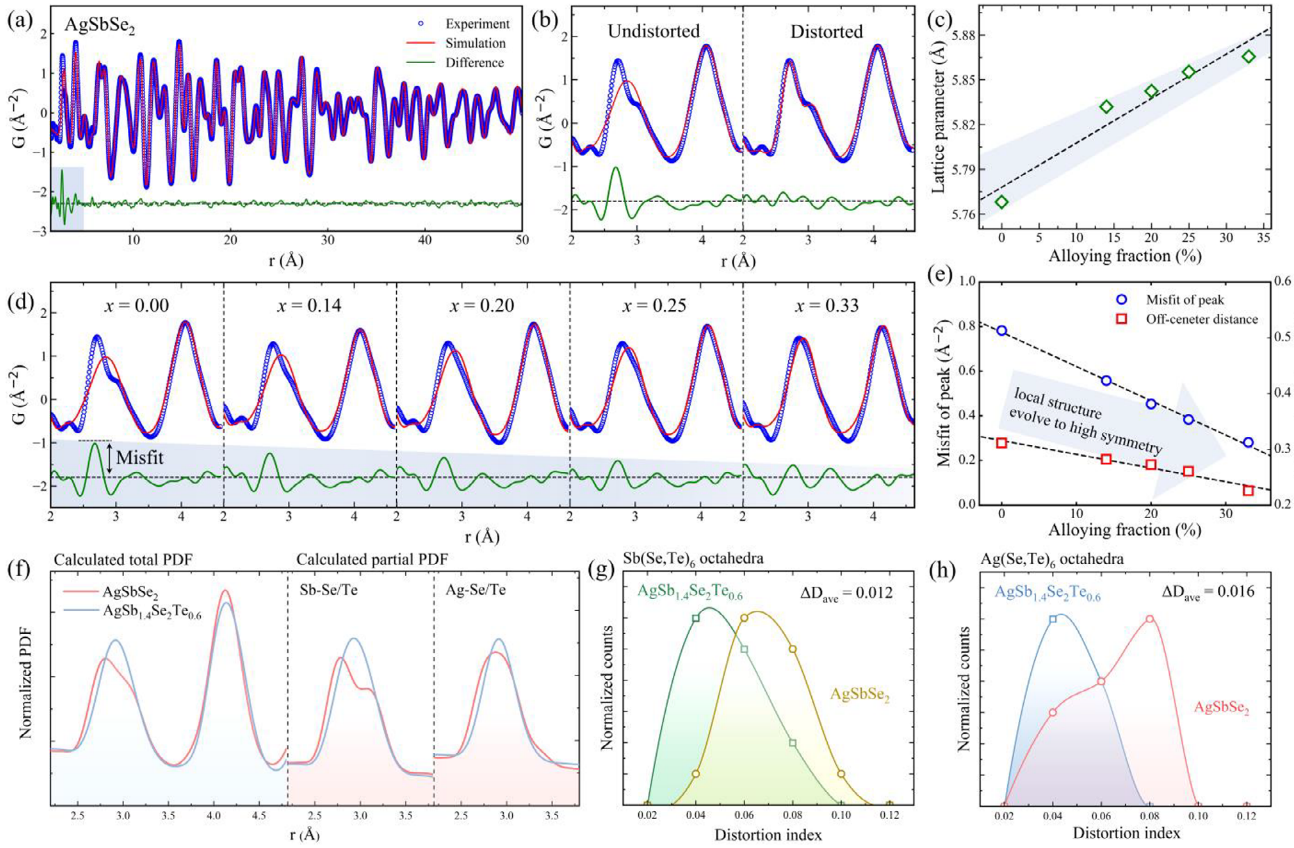

FIGURE 2 | (a), (b) The (a) average and (b) local atomic structure PDF refinements with the undistorted cubic and [111]-distorted models of the pristine AgSbSe$_2$ sample. The experiment data, structural model simulation, and difference are shown in blue, red, and green curves, respectively. The goodness-of-fit parameter is $R_w = 0.1073$. Detailed information on PDF structural refinements can be found in Figures S5 and S6, Tables S2–S4. (c) The lattice parameter of AgSb$_{1+2x}$Se$_2$Te$_{3x}$ ($0.0 \le x \le 0.33$) obtained from PDF structural refinements. (d) The local structure refinements of AgSb$_{1+2x}$Se$_2$Te$_{3x}$ ($0.0 \le x \le 0.33$) with the undistorted cubic model over the range of $2.0 < r < 4.6$ Å. (e) The local structure misfit value of the undistorted cubic model in the first PDF peak and the off-center distance from cubic [111] distorted model refinements. (f) The total and partial PDF calculated from DFT relaxed crystal models of AgSbSe$_2$ and AgSb$_{1.4}$Se$_2$Te$_{0.6}$. (g), (h) The distortion index distribution of (g) Sb(Se,Te)$_6$ octahedra and (h) Ag(Se, Te)$_6$ octahedra. The ΔD$_{ave}$ parameter represents the change in the average value of the distortion index.

local structural distortion beyond the averaged cubic symmetry is observed. As shown in Figure 2d, the misfit of the first peak is still evident with the undistorted cubic model, but it decreases gradually with the increase of Sb$_2$Te$_3$ alloying. The misfit values and refined off-center distance are shown together in Figure 2e. It suggests that local structural distortions caused by lone pair electrons are weakened during alloying. The local structure of alloyed AgSbSe$_2$ gradually transforms into the average structure with higher symmetry. The Raman spectra (Figure S7) reconcile well with the local symmetry evolution unveiled by PDF analysis, where the low-energy optical phonon modes (<100 cm^{-1}) are Raman-forbidden in the rock-salt cubic symmetry. With the increase of alloying fraction, the peaks of low-energy optical phonon modes become weaker, validating that the local structure evolves to higher symmetry.

The alloying introduced defects would interact with the lone pair electron effects, which can contribute to the local structure evolution during alloying. To further validate the physical mechanism of local structure evolution, the density functional theory (DFT) calculations were carried out with Quantum ESPRESSO [52, 53] using Perdew-Burke-Ernzerhof (PBE) exchange-correlation function [54]. In Figure 2f, the total and partial PDFs are calculated from the DFT relaxed models (Figure S8), which are in good agreement with the experimental PDF data. Comparing AgSbSe$_2$ and AgSb$_{1.4}$Se$_2$Te$_{0.6}$, the total PDF peaks become much broadened due to the alloying, and only the Sb-Se/Te partial PDF shows a peak split, suggesting the contribution of lone pair electrons onto the local structure. It is noteworthy that the change of peak shape after alloying is closely related to the defects in the local structure. The distortion index of octahedra was calculated to describe the local structural distortion contributed from defects and lone pair electron effects. When alloying with Sb$_2$Te$_3$, cationic vacancy and anionic disordering are introduced into the atomic structure. The larger ionic radius of Te (221 pm) can enhance the chemical bonding inhomogeneity of octahedra, maintaining a larger octahedra distortion in Sb(Se,Te)$_6$ (Figure S9a). However, the vacancies reduce the neighboring octahedra distortion (Figure S9b), resulting in the suppression of local atomic off-centering. The distribution of the distortion index for octahedra in DFT models is shown in Figure 2g,h, where all octahedra become less distorted after alloying, revealing that the introduced vacancies dominate the distortion variation. The pristine large distortion contributed by lone pair electron effects of Sb^{3+} was weakened by the introduction of vacancies, leading to the evolution of local structure to higher symmetry.

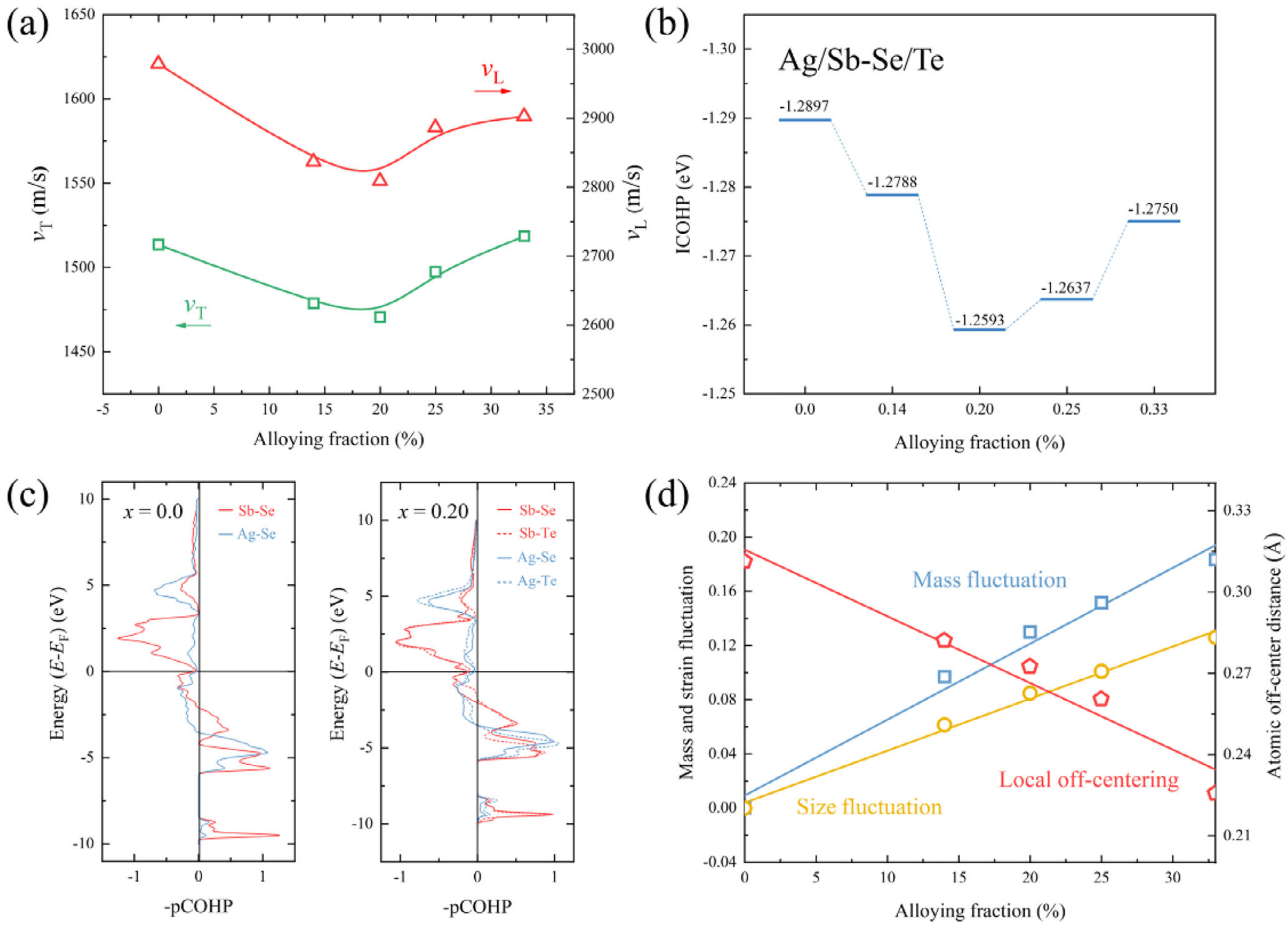

FIGURE 3 | (a) The alloying-fraction-dependent longitudinal (v_L) and transverse (v_T) sound velocities of $AgSb_{1+2x}Se_2Te_{3x}$ ($0.0 \leq x \leq 0.33$). (b) The alloying-fraction-dependent ICOHP value of Ag/Sb-Se/Te bonding. (c) The pCOHP patterns of $AgSbSe_2$ (left) and $AgSb_{1.4}Se_2Te_{0.6}$ (right). (d) The mass fluctuation, size fluctuation, and local off-center distance of $AgSb_{1+2x}Se_2Te_{3x}$ ($0.0 \leq x \leq 0.33$).

Structure manipulation through alloying has been demonstrated as an effective strategy to soften chemical bonds and decrease κ_L to obtain promising thermoelectric performance [55]. At the atomic level, the sound velocity can be influenced by the change of chemical bond strength [56, 57]. In order to further understand the κ_L variation, the acoustic properties were measured to show the longitudinal and transverse sound velocity variation during alloying (Figure 3a). The acoustic properties variation was in good agreement with κ_L, suggesting that the κ_L was mainly determined by the sound velocity during alloying. The integrated crystal orbital Hamilton population (ICOHP) calculation was carried out to investigate the bonding strength variation (Figure 3b), where the stronger bonding strength corresponds to more negative values. The bonding strength decreases in the samples of $x = 0$, 0.14, and 0.20, while it increases in those of $x = 0.25$ and 0.33. This tendency matches well with sound velocity change, leading to lattice softening. The atomic off-centering and composition-dependent ICOHP results further illustrate the effect of structure manipulation on chemical bonding strength (Figure S10). The partial crystal orbital Hamilton population (pCOHP) results (Figure 3c) also indicate that the bonding state moves closer to the Fermi level after alloying, revealing the decreased stability of the bonding orbital, leading to the weakening of bonding strength.

To better understand the structural origin of the variation in lattice thermal conductivity, the mass and size fluctuations were calculated during Sb_2Te_3 alloying. As shown in Figure 3d, the mass fluctuation, size fluctuation, and bonding heterogeneity were significantly increased due to the introduced cationic vacancy and anionic disorder. These effects would typically strengthen phonon scattering and thereby suppress the lattice thermal conductivity. However, the observed trend in lattice thermal conductivity contradicts the expectation from conventional defect engineering, indicating that thermal transport in this system is not simply ruled by defect engineering. Considering the local structure evolution from PDF results, the local structure with higher symmetry would reduce the lattice anharmonicity during alloying [18]. The theoretical calculation confirmed that the reduction of the Sb off-centering distance increases the sound velocity (Figure S11), resulting in the rise of lattice thermal conductivity. Thus, combining theoretical analysis with experimental results reveals that the sound velocity variation is the result of competition between the mass and size fluctuations, caused by introduced defects and local structure atomic off-centering, leading to the change of lattice thermal conductivity. At low alloying concentrations ($x = 0.14$ and 0.20), the enhanced mass and size fluctuations dominate, leading to a decrease in lattice thermal conductivity, while at higher concentrations ($x = 0.25$

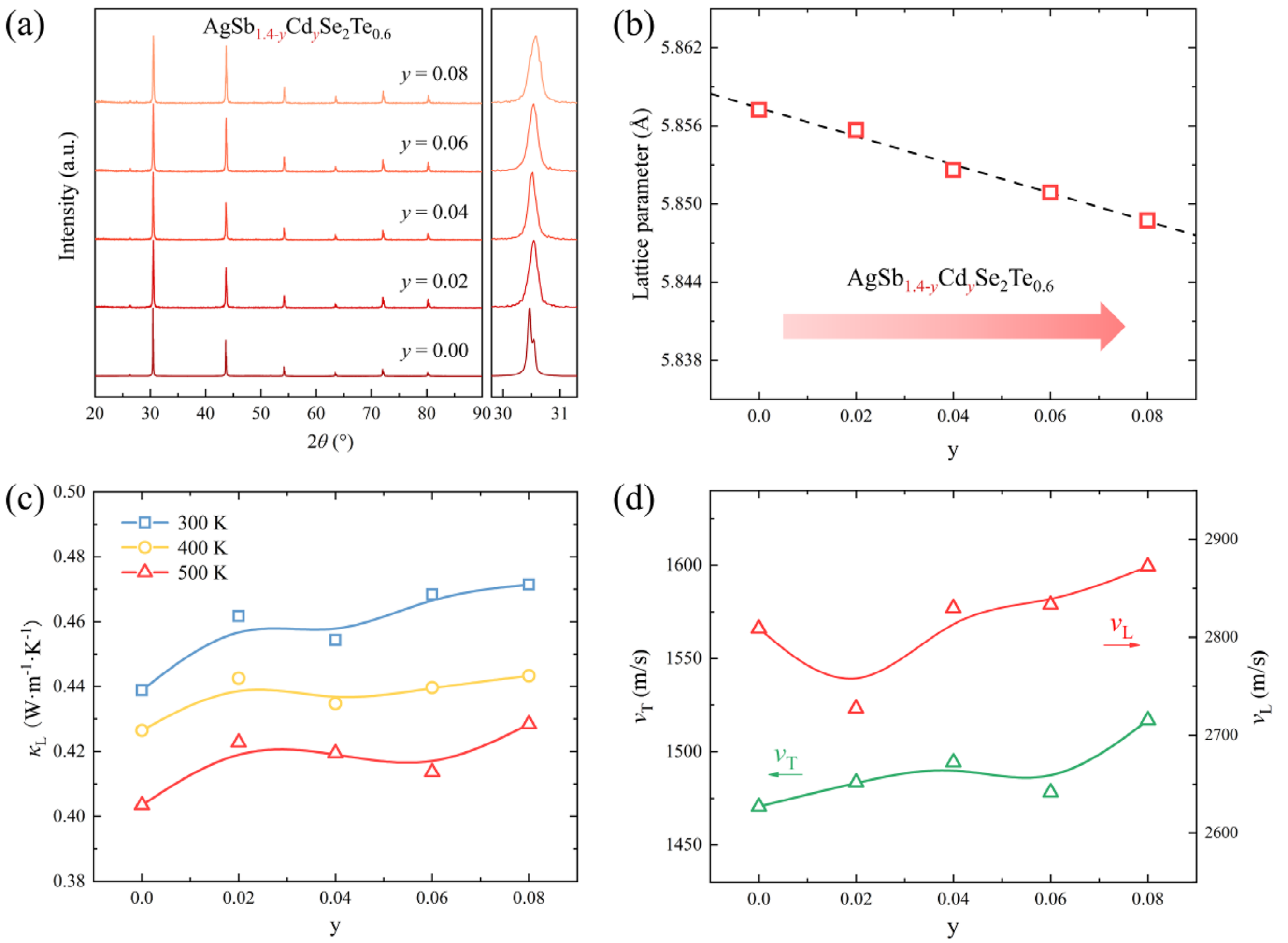

FIGURE 4 | (a) Room-temperature powder XRD patterns of $AgSb_{1.4\text{-}y}Cd_ySe_2Te_{0.6}$ ($0.0 \leq y \leq 0.08$). (b) Room-temperature lattice parameters of $AgSb_{1.4\text{-}y}Cd_ySe_2Te_{0.6}$ ($0.0 \leq y \leq 0.08$) obtained from XRD Rietveld refinements. Detailed information on Rietveld refinements can be found in Figure S13 and Table S5. (c) The experimental lattice thermal conductivities at 300, 400, and 500 K of $AgSb_{1.4\text{-}y}Cd_ySe_2Te_{0.6}$ ($0.0 \leq y \leq 0.08$). (d) The alloying-fraction-dependent longitudinal (ν_L) and transverse (ν_T) sound velocities of $AgSb_{1.4\text{-}y}Cd_ySe_2Te_{0.6}$ ($0.0 \leq y \leq 0.08$). The temperature depended κ_L of $AgSb_{1.4\text{-}y}Cd_ySe_2Te_{0.6}$ ($0.0 \leq y \leq 0.08$) was shown in Figure S14a.

and 0.33), the reduction in lone pair electrons outweighs the mass and size fluctuations, resulting in an increase in lattice thermal conductivity.

Considering the temperature independence of κ_L (Figure S12a) and the atomic off-centering behavior of Sb in $AgSbSe_2$, the phonon behavior of this system deviates from the conventional Umklapp-dominated tendency. Therefore, the diffusive thermal conductivity (κ_{diff}) model [58] was applied to explore the κ_L variation, which can better describe the heat transfer behavior in materials with high atomic disorder, complex crystal structures, and ultralow thermal conductivity [59]. The diffusive thermal conductivity can be described by the following equation:

$$\kappa_{\text{diff}} = 0.76 n^{\frac{2}{3}} k_B \frac{1}{3} (2\nu_T + \nu_L) \tag{1}$$

where n is the experimental number density of atoms, k_B is the Boltzmann constant, and ν_T and ν_L is the transverse and longitudinal sound velocity, respectively. The calculated κ_{diff} is shown in Figure S12b, and compared with κ_L at 550 K and κ_{min} estimated via the Debye-Cahill model [60]. The κ_L of alloyed $AgSb_{1.4}Se_2Te_{0.6}$ at 550 K is approaching the κ_{min}, revealing the introduced defects, anionic disordering, and lone pair electron effects create a complex local environment for thermal transport.

In order to better understand the local structure evolution affected by the substitution of group V element with lone pair electrons, the Cd element, which has no lone pair electrons, replaces Sb in $AgSb_{1.4\text{-}y}Cd_ySe_2Te_{0.6}$ ($0.0 \leq y \leq 0.08$). The ionic radius of Cd^{2+} is 95 pm, which is larger than that of Sb^{3+} (76 pm). Conventionally, the atomic substitution with a larger ionic radius usually expands the lattice, increases phonon scattering, and reduces the lattice thermal conductivity. However, the XRD pattern in Figure 4a shows that the Bragg peak moves to higher angles, suggesting an uncommon negative lattice expansion, which is also verified by the quantitative modeling results from Rietveld refinements (Figure 4b). The lattice thermal conductivity (Figure 4c) also increases with more Cd doping, which is related to the increase in sound velocities (Figure 4d). To

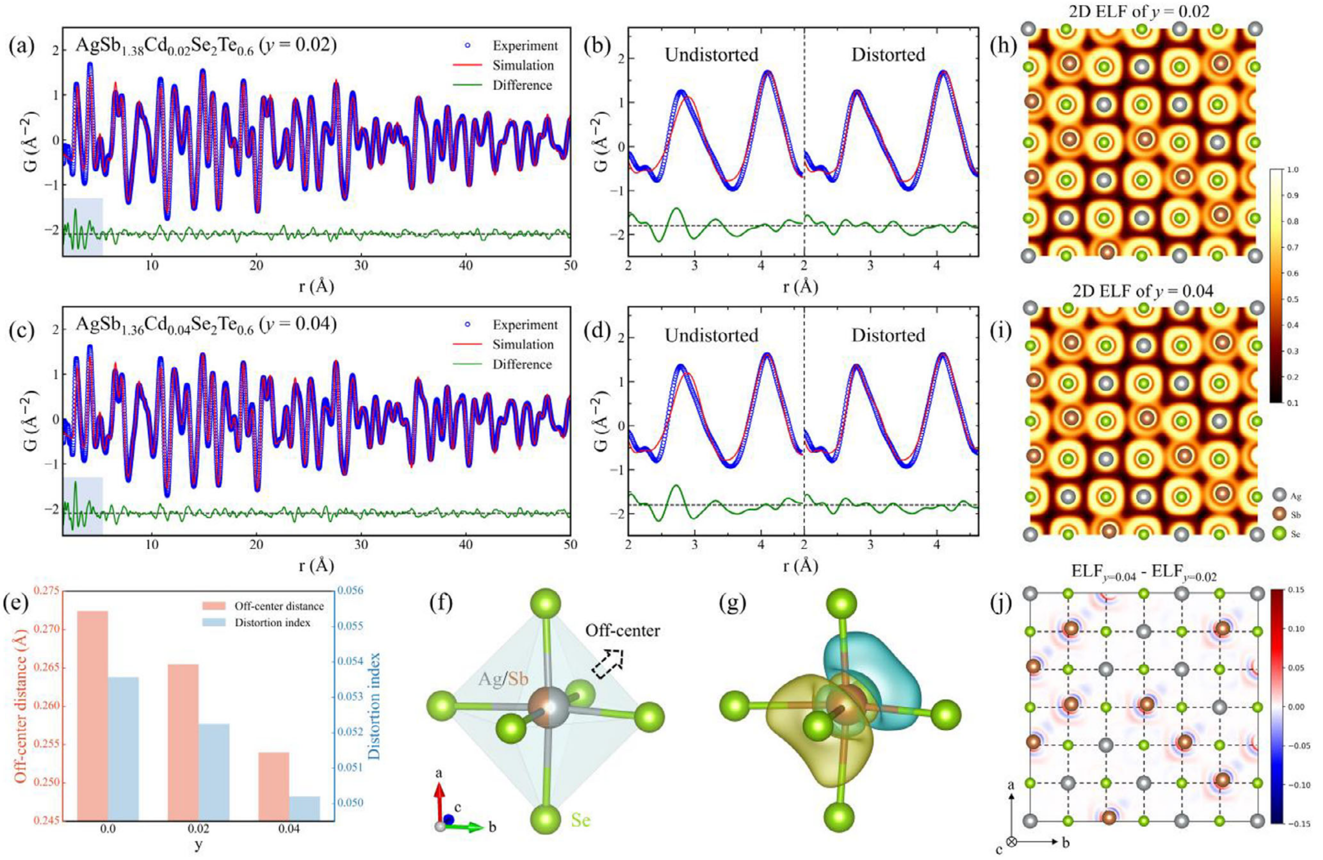

FIGURE 5 | (a), (c) The average structure PDF refinements of (a) $AgSb_{1.38}Cd_{0.02}Se_2Te_{0.6}$ ($y = 0.02$) and (c) $AgSb_{1.36}Cd_{0.04}Se_2Te_{0.6}$ ($y = 0.04$). The experiment data, structural model simulation, and difference are shown in blue, red, and green curves, respectively. (b), (d) The local structure refinements of (b) $AgSb_{1.38}Cd_{0.02}Se_2Te_{0.6}$ ($y = 0.02$) and (d) $AgSb_{1.36}Cd_{0.04}Se_2Te_{0.6}$ ($y = 0.04$) with undistorted cubic and [111] distorted model over the range of $2.0 < r < 4.6$. Detailed information on PDF structural refinements can be found in Tables S6 and S7. (e) Local atomic off-center displacement and distortion index of $(Ag,Sb)Se_6$ octahedra. (f) The local atomic off-center displacement of cation in the $(Ag,Sb)Se_6$ octahedra. (g) The DFT calculated charge density difference between $AgSb_{1.38}Cd_{0.02}Se_2Te_{0.6}$ and $AgSb_{1.36}Cd_{0.04}Se_2Te_{0.6}$.(h), (i) The 2D ELF slices of (h) $AgSb_{1.38}Cd_{0.02}Se_2Te_{0.6}$ ($y = 0.02$) and (i) $AgSb_{1.36}Cd_{0.04}Se_2Te_{0.6}$ ($y = 0.04$). (j) The 2D ELF difference between $AgSb_{1.38}Cd_{0.02}Se_2Te_{0.6}$ and $AgSb_{1.36}Cd_{0.04}Se_2Te_{0.6}$.

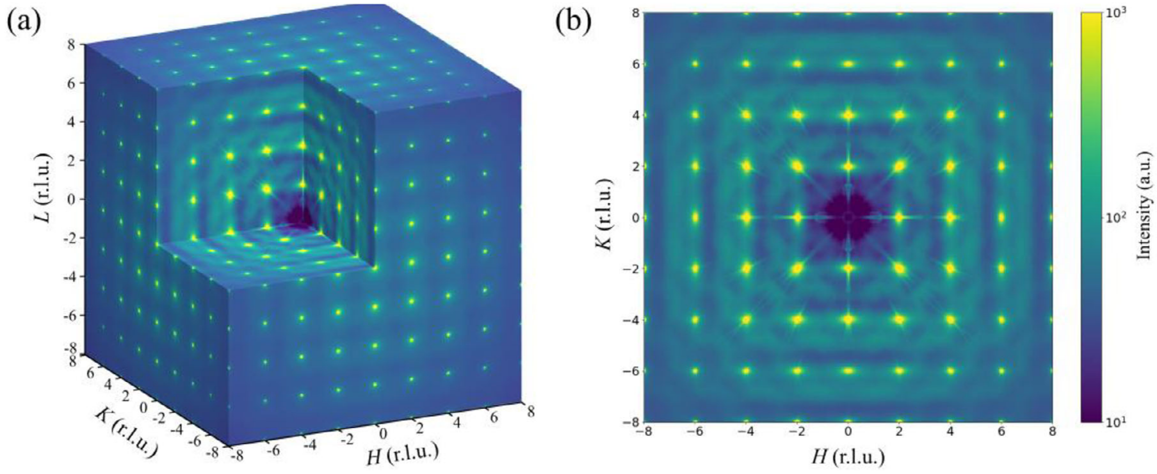

FIGURE 6 | (a) The 3D volume of X-ray diffuse scattering at 300 K. (b) The X-ray diffuse scattering of the $AgSbSe_2$ single crystal in the reciprocal space $\mathbf{Q} = (HK0)$ plane at 300 K, displayed in reciprocal lattice units (r.l.u.).

validate the phase purity, SEM observation and EDS analysis of the $AgSb_{1.4\text{-}y}Cd_ySe_2Te_{0.6}$ ($y = 0.02$) are shown in Figure S15, confirming no impurity phases. The total and electronic thermal conductivities during Cd doping are shown in Figure S14b,c, respectively. The total thermal conductivity remains dominantly contributed by lattice thermal conductivity. This unusual change, in both atomic structures and thermal transport properties, supports our argument in the $AgSbSe_2$-Sb_2Te_3 alloying system that the local structure evolution will affect the heat transport performance, as attributed to the group V element content.

The X-ray PDF local structure analysis was performed on $AgSb_{1.38}Cd_{0.02}Se_2Te_{0.6}$ ($y = 0.02$) and $AgSb_{1.36}Cd_{0.04}Se_2Te_{0.6}$ ($y = 0.04$), to further study the influence of Sb^{3+} substitution on the local structures. While the average structure was kept as cubic symmetry in both materials, the lone pair electrons induced off-centering was also observed in the local structure (Figure 5a–d). To describe the local structural distortions quantitatively, the cation off-center displacement and octahedra distortion index are obtained from PDF analysis. As shown in Figure 5e, with the increase of Cd doping, the local atomic off-center displacement decreases, and the $(Ag,Sb)Se_6$ octahedra become less distorted. The local structure of material evolves to higher symmetry. As a sanity check, similar PDF analysis results were also verified by the lab-source X-ray PDF experiment (Figure S16 and Tables S8 and S9). During the Cd substitution, the mass and size fluctuations were insignificant (Figure S17). The decrease in the concentration of distorted $SbSe_6$ octahedra results in a significant local off-center distance change, leading to the increase of sound velocity and lattice thermal conductivity.

Based on the local structure model obtained from the PDF analysis, the DFT calculations of electron localization function (ELF) and charge density difference were carried out. The evolution of local structure is closely related to the charge arrangement among atoms. As shown in Figure 5f,g, the charge difference in the octahedra is mainly due to the cationic off-center deviations, in which the charges are rearranged along the [111] direction, which aligns well with the PDF local structure analysis results. The 2D ELF difference also confirms the charge re-distribution near Sb^{3+} (Figure 5h–j). It gives a straightforward demonstration of the connection between 3D charge arrangement and atomic off-centering, which explains the influence of local structure evolution on κ_L. Considering that the lattice thermal conductivity is highly related to the Sb content, increasing the Sb concentration or substituting Ag with group V elements would be a promising strategy to enhance phonon scattering in the $AgSbSe_2$ system.

The intrinsic local symmetry breaking in $AgSbSe_2$ would give rise to diffuse scattering, which represents the structural deviations from the averaged crystallographic structure. To validate this, the newly developed 3D X-ray diffuse scattering technique is carried out to collect diffuse scattering signals of the $AgSbSe_2$ single crystal over the full 3D reciprocal space [61]. The single crystal PDF data was processed using the software packages NXRefine and CCTW (Crystal Coordinate Transformation Workflow) within NeXpy [62–64]. More detailed experimental information can be found in the Supporting Information. The 3D volume of X-ray diffuse scattering data is transformed and represented in *HKL* reciprocal space coordinates (Figure 6a), in which the bright Bragg peaks present the averaged crystallographic structure information, aligning well with reported long-range cubic structure [40], confirming the high quality of synthesized $AgSbSe_2$ single crystal. More importantly, significant diffuse scattering is observed over the full reciprocal space, indicating that the local structure has a different atomic arrangement from the long-range cubic structure. Taking the $\mathbf{Q} = (HK0)$ plane as an example (Figure 6b), the diffuse rods are evident between Bragg peaks, which is a direct observation on the local structure distortions in $AgSbSe_2$. This provides a new structural insight for studying the short-range ordering in high-symmetry materials, as induced by lone pair electrons, which is usually hidden in conventional long-range structural analysis.

3 | Conclusion

In this work, the local structure manipulation was achieved by alloying $AgSbSe_2$ with the non-equiatomic Sb_2Te_3, introducing defects to study the nanoscale local distortion evolution and κ_L variation. The powder X-ray pair distribution function analysis was performed to investigate the local structure evolution during alloying quantitatively, which reveals the reduction of lone pair electron effects. Furthermore, the Cd substitution on Sb^{3+} site was introduced in the system to manipulate lone pair electrons, revealing that the decrease of lone pair electron effects will lead to a loss of short-range distortion. Combined with DFT calculation and theoretical analysis, the anionic alloying and lone pair electron effects variation are confirmed to influence the chemical bonding strength leading to the change of sound velocity, and the lone pair electron effects can be suppressed by controlling the content of vacancies and group V elements in the material, which enables the local structure to be higher symmetry. Furthermore, a direct visualization of diffuse scattering in the $AgSbSe_2$ single crystal is achieved, revealing the intrinsic nanoscale local symmetry breaking in the local structure, which is the key to retain low κ_L. This work provides a local-structure-oriented strategy for designing I-V-VI_2 compounds with lone pair electron effects to achieve low κ_L for thermoelectric applications.

Acknowledgements

This work was supported by the National Natural Science Foundation of China (Grant Nos. 52302193 and 52371234), the Hong Kong, Macao, and Taiwan Science and Technology Cooperation Project for Science and Technology Innovation Plan of Shanghai (23520760600), and the Fundamental Research Funds for the Central Universities. The authors acknowledge the Instrument Analysis Center of Tongji University. The authors thank the Shanghai Synchrotron Radiation Facility of BL12SW (https://cstr.cn/31124.02.SSRF.BL12SW) for the assistance on X-ray PDF measurements (Proposal No. 2023-SSRF-PT-504692).

Conflicts of Interest

The authors declare no conflicts of interest.

Data Availability Statement

The data that support the findings of this study are available from the corresponding author upon reasonable request.

References

1. Y. Wu, Z. Chen, P. Nan, et al., "Lattice Strain Advances Thermoelectrics," *Joule* 3 (2019): 1276–1288, https://doi.org/10.1016/j.joule.2019.02.008.

2. Z. Chen, Z. Jian, W. Li, et al., "Lattice Dislocations Enhancing Thermoelectric PbTe in Addition to Band Convergence," *Advanced Materials* 29 (2017): 1606768, https://doi.org/10.1002/adma.201606768.

3. B. Poudel, Q. Hao, Y. Ma, et al., "High-Thermoelectric Performance of Nanostructured Bismuth Antimony Telluride Bulk Alloys," *Science* 320 (2008): 634–638, https://doi.org/10.1126/science.1156446.

4. R. Deng, X. Su, S. Hao, et al., "High Thermoelectric Performance in $Bi_{0.46}Sb_{1.54}Te_3$ Nanostructured With ZnTe," *Energy & Environmental Science* 11 (2018): 1520–1535, https://doi.org/10.1039/C8EE00290H.

5. Y. Xiao, Y. Wu, P. Nan, et al., "Cu Interstitials Enable Carriers and Dislocations for Thermoelectric Enhancements in n-$PbTe_{0.75}Se_{0.25}$," *Chemistry* 6 (2020): 523–537, https://doi.org/10.1016/j.chempr.2020.01.002.

6. Z. Chen, B. Ge, W. Li, et al., "Vacancy-Induced Dislocations Within Grains For High-Performance PbSe Thermoelectrics," *Nature Communications* 8 (2017): 13828, https://doi.org/10.1038/ncomms13828.

7. W. Li, S. Lin, M. Weiss, et al., "Crystal Structure Induced Ultralow Lattice Thermal Conductivity in Thermoelectric Ag_9AlSe_6," *Advanced Energy Materials* 8 (2018): 1800030, https://doi.org/10.1002/aenm.201800030.

8. K. Pal, X. Hua, Y. Xia, and C. Wolverton, "Unraveling the Structure-Valence-Property Relationships in $AMM'Q_3$ Chalcogenides With Promising Thermoelectric Performance," *ACS Applied Energy Materials* 3 (2020): 2110–2119, https://doi.org/10.1021/acsaem.9b02139.

9. M. D. Nielsen, V. Ozolins, and J. P. Heremans, "Lone Pair Electrons Minimize Lattice Thermal Conductivity," *Energy & Environmental Science* 6 (2013): 570–578, https://doi.org/10.1039/C2EE23391F.

10. H. Xie, E. S. Bozin, Z. Li, et al., "Hidden Local Symmetry Breaking in Silver Diamondoid Compounds is Root Cause of Ultralow Thermal Conductivity," *Advanced Materials* 34 (2022): 2202255, https://doi.org/10.1002/adma.202202255.

11. J. Su, Y. Liu, Y. Li, et al., "Intrinsic Off-Centering and Light Conduction Band Structure Lead to High Thermoelectric Performance in N-Type Diamondoid $AgInSe_2$," *Journal of the American Chemical Society* 147 (2025): 16611–16619, https://doi.org/10.1021/jacs.5c04294.

12. H. Xie, Z. Li, Y. Liu, et al., "Silver Atom Off-Centering in Diamondoid Solid Solutions Causes Crystallographic Distortion and Suppresses Lattice Thermal Conductivity," *Journal of the American Chemical Society* 145 (2023): 3211–3220, https://doi.org/10.1021/jacs.2c13179.

13. T. Jin, L. Yang, D. Zhang, et al., "Designing Semiconductors From the Assembly of Close-Packed Slabs," *Chemistry of Materials* 36 (2024): 11189–11199, https://doi.org/10.1021/acs.chemmater.4c02062.

14. D. Zhang, M. Liu, T. Jin, L. Yang, W. Li, and Y. Pei, "$(AgSbTe_2)_{1\text{-}x}(Bi2Te_3)_x$-based thermoelectric device for low-grade heat recovery," *Materials Today Physics* 52 (2025): 101692.

15. D. T. Morelli, V. Jovovic, and J. P. Heremans, "Intrinsically Minimal Thermal Conductivity in Cubic I–V–VI_2 Semiconductors," *Physical Review Letters* 101 (2008): 035901, https://doi.org/10.1103/PhysRevLett.101.035901.

16. J. Ma, O. Delaire, A. F. May, et al., "Glass-Like Phonon Scattering From A Spontaneous Nanostructure In $AgSbTe_2$," *Nature Nanotechnology* 8 (2013): 445–451, https://doi.org/10.1038/nnano.2013.95.

17. N. Rezaei, S. J. Hashemifar, and H. Akbarzadeh, "Thermoelectric Properties of $AgSbTe_2$ From First-Principles Calculations," *Journal of Applied Physics* 116 (2014): 103705, https://doi.org/10.1063/1.4895062.

18. M. Dutta, M. V. D. Prasad, J. Pandey, A. Soni, U. V. Waghmare, and K. Biswas, "Local Symmetry Breaking Suppresses Thermal Conductivity in Crystalline Solids," *Angewandte Chemie International Edition* 61 (2022): 202200071, https://doi.org/10.1002/anie.202200071.

19. H. Jang, M. Y. Toriyama, S. Abbey, et al., "Suppressed Lone Pair Electrons Explain Unconventional Rise of Lattice Thermal Conductivity in Defective Crystalline Solids," *Advanced Science* 11 (2024): 2308075, https://doi.org/10.1002/advs.202308075.

20. K. Zhang, Y. Huang, S. Liu, et al., "Direct Experimental Evidence of Low Carrier Scattering Potential in High Performance Thermoelectric $AgSbSe_2$ Crystal," *Advanced Materials* 37 (2025): 2503496, https://doi.org/10.1002/adma.202503496.

21. S. N. Guin, A. Chatterjee, D. S. Negi, R. Datta, and K. Biswas, "High Thermoelectric Performance In Tellurium Free p-type $AgSbSe_2$," *Energy & Environmental Science* 6 (2013): 2603, https://doi.org/10.1039/c3ee41935e.

22. C. Xiao, X. Qin, J. Zhang, et al., "High Thermoelectric and Reversible p-n-p Conduction Type Switching Integrated in Dimetal Chalcogenide," *Journal of the American Chemical Society* 134 (2012): 18460–18466, https://doi.org/10.1021/ja308936b.

23. Y. Li, J. Su, Y. Wen, et al., "Realizing High ZT_{ave} in N-Type Diamondoid $AgInSe_2$ Thermoelectrics via Lone-Pair Electrons and Isomorphous Alloy," *Small* 21 (2025): 2506188.

24. H. Xie, X. Su, S. Hao, et al., "Large Thermal Conductivity Drops in the Diamondoid Lattice of $CuFeS_2$ by Discordant Atom Doping," *Journal of the American Chemical Society* 141 (2019): 18900–18909, https://doi.org/10.1021/jacs.9b10983.

25. M. K. Jana, K. Pal, U. V. Waghmare, and K. Biswas, "The Origin of Ultralow Thermal Conductivity in InTe: Lone-Pair-Induced Anharmonic Rattling," *Angewandte Chemie* 128 (2016): 7923–7927, https://doi.org/10.1002/ange.201511737.

26. M. Dutta, S. Matteppanavar, M. V. D. Prasad, et al., "Rattling," *Journal of the American Chemical Society* 141 (2019): 20293–20299, https://doi.org/10.1021/jacs.9b10551.

27. D. Wan, S. Bai, S. Fan, et al., "Strain-Driven Lone Pair Electron Expression For Thermal Transport in BiCuSeO," *Nature Communications* 16 (2025): 6284, https://doi.org/10.1038/s41467-025-61506-6.

28. X. Huang, X. Li, Y. Tao, et al., "Understanding Electron–Phonon Interactions in 3D Lead Halide Perovskites From the Stereochemical Expression of $6s^2$ Lone Pairs," *Journal of the American Chemical Society* 144 (2022): 12247–12260, https://doi.org/10.1021/jacs.2c03443.

29. D. H. Fabini, G. Laurita, J. S. Bechtel, et al., "Dynamic Stereochemical Activity of the Sn^{2+} Lone Pair in Perovskite $CsSnBr_3$," *Journal of the American Chemical Society* 138 (2016): 11820–11832, https://doi.org/10.1021/jacs.6b06287.

30. O. Cherniushok, R. Cardoso-Gil, T. Parashchuk, R. Knura, Y. Grin, and K. T. Wojciechowski, "Lone-Pair-Like Interaction and Bonding Inhomogeneity Induce Ultralow Lattice Thermal Conductivity in Filled β-Manganese-Type Phases," *Chemistry of Materials* 34 (2022): 6389–6401, https://doi.org/10.1021/acs.chemmater.2c00915.

31. L. Agnarelli, Y. Prots, R. Ramlau, et al., "$Mg_{29-x}Pt_{4+y}$: Chemical Bonding Inhomogeneity and Structural Complexity," *Inorganic Chemistry* 61 (2022): 16148–16155, https://doi.org/10.1021/acs.inorgchem.2c02653.

32. N. Sato, N. Kuroda, S. Nakamura, et al., "Bonding Heterogeneity In Mixed-Anion Compounds Realizes Ultralow Lattice Thermal Conductivity," *Journal of Materials Chemistry A* 9 (2021): 22660–22669, https://doi.org/10.1039/D1TA04958E.

33. Y. Grin, "Inhomogeneity And Anisotropy Of Chemical Bonding And Thermoelectric Properties Of Materials," *Journal of Solid State Chemistry* 274 (2019): 329–336, https://doi.org/10.1016/j.jssc.2018.12.055.

34. Z. Xia, X. Shen, J. Zhou, et al., "Realizing Intrinsically Ultralow and Glass-Like Thermal Transport via Chemical Bonding Engineering," *Advanced Science* 12 (2025): 2417292, https://doi.org/10.1002/advs.202417292.

35. Y. Grin, A. Savin, and B. Silvi, *The Chemical Bond*, eds. G. Frenking and S. Shaik (Wiley, 2014), 345–382, https://doi.org/10.1002/9783527664696.

36. T. Weber and A. Simonov, “The Three-Dimensional Pair Distribution Function Analysis Of Disordered Single Crystals: Basic Concepts,” *Zeitschrift für Kristallographie* 227 (2012): 238–247, https://doi.org/10.1524/zkri.2012.1504.

37. A. Simonov, T. De Baerdemaeker, H. L. B. Boström, et al., “Hidden Diversity Of Vacancy Networks In Prussian Blue Analogues,” *Nature* 578 (2020): 256–260, https://doi.org/10.1038/s41586-020-1980-y.

38. B. Sangiorgio, E. S. Bozin, C. D. Malliakas, et al., “Correlated Local Dipoles In PbTe,” *Physical Review Materials* 2 (2018): 085402, https://doi.org/10.1103/PhysRevMaterials.2.085402.

39. T. Kang, C. Li, X. Zhang, et al., “Local Symmetry Breaking Induced Superionic Conductivity in Argyrodites,” *Journal of the American Chemical Society* 148 (2026): 6158–6166, https://doi.org/10.1021/jacs.5c17193.

40. S. Geller and J. H. Wernick, “Ternary Semiconducting Compounds With Sodium Chloride-Like Structure: $AgSbSe_2$, $AgSbTe_2$, $AgBiS_2$, $AgBiSe_2$,” *Acta Crystallographica* 12 (1959): 46–54, https://doi.org/10.1107/S0365110X59000135.

41. W. Gao, Z. Wang, J. Huang, and Z. Liu, “Extraordinary Thermoelectric Performance Realized in Hierarchically Structured $AgSbSe_2$ With Ultralow Thermal Conductivity,” *ACS Applied Materials & Interfaces* 10 (2018): 18685–18692, https://doi.org/10.1021/acsami.8b03243.

42. L.-H. Ye, K. Hoang, A. J. Freeman, et al., “First-Principles Study Of The Electronic, Optical, And Lattice Vibrational Properties Of $AgSbTe_2$,” *Physical Review B* 77 (2008): 245203, https://doi.org/10.1103/PhysRevB.77.245203.

43. R. D. Shannon, “Revised Effective Ionic Radii And Systematic Studies Of Interatomic Distances In Halides And Chalcogenides,” *Acta Crystallographica Section A* 32 (1976): 751–767, https://doi.org/10.1107/S0567739476001551.

44. B. H. Toby and R. B. Von Dreele, “GSAS-II: The Genesis Of A Modern Open-Source All Purpose Crystallography Software Package,” *Journal of Applied Crystallography* 46 (2013): 544–549, https://doi.org/10.1107/S0021889813003531.

45. T. Egami and S. J. L. Billinge, *Underneath the Bragg peaks: Structural analysis of complex materials*, 2nd edition (Elsevier, 2012).

46. S. J. L. Billinge, S. H. Skjaervoe, M. W. Terban, et al., *Comprehensive Inorganic Chemistry III* (Elsevier, 2023), 222–247.

47. K. Yang, Z.-H. Dong, C.-Y. Zhou, et al., “Ultrahard X-Ray Multifunctional Application Beamline At The SSRF,” *Nuclear Science and Techniques* 35 (2024): 98, https://doi.org/10.1007/s41365-024-01468-4.

48. P. J. Chupas, X. Qiu, J. C. Hanson, P. L. Lee, C. P. Grey, and S. J. L. Billinge, “Rapid-Acquisition Pair Distribution Function (RA-PDF) Analysis,” *Journal of Applied Crystallography* 36 (2003): 1342–1347, https://doi.org/10.1107/S0021889803017564.

49. J. Kieffer and D. Karkoulis, “PyFAI, A Versatile Library For Azimuthal Regrouping,” *Journal of Physics: Conference Series* 425 (2013): 202012, https://doi.org/10.1088/1742-6596/425/20/202012.

50. P. Juhás, T. Davis, C. L. Farrow, and S. J. L. Billinge, “PDFgetX3: A Rapid And Highly Automatable Program For Processing Powder Diffraction Data Into Total Scattering Pair Distribution Functions,” *Journal of Applied Crystallography* 46 (2013): 560–566, https://doi.org/10.1107/S0021889813005190.

51. T. Proffen and S. J. L. Billinge, “PDFFIT, A Program For Full Profile Structural Refinement Of The Atomic Pair Distribution Function,” *Journal of Applied Crystallography* 32 (1999): 572–575, https://doi.org/10.1107/S0021889899003532.

52. G. Kresse and D. Joubert, “From Ultrasoft Pseudopotentials To The Projector Augmented-Wave Method,” *Physical Review B* 59 (1999): 1758–1775, https://doi.org/10.1103/PhysRevB.59.1758.

53. G. Kresse and J. Furthmüller, “Efficiency Of Ab-Initio Total Energy Calculations For Metals And Semiconductors Using A Plane-Wave Basis Set,” *Computational Materials Science* 6 (1996): 15–50, https://doi.org/10.1016/0927-0256(96)00008-0.

54. J. P. Perdew, K. Burke, and M. Ernzerhof, “Generalized Gradient Approximation Made Simple,” *Physical Review Letters* 77 (1996): 3865–3868, https://doi.org/10.1103/PhysRevLett.77.3865.

55. A. R. Muchtar, B. Srinivasan, S. L. Tonquesse, et al., “Physical Insights on the Lattice Softening Driven Mid-Temperature Range Thermoelectrics of Ti/Zr-Inserted SnTe—An Outlook Beyond the Horizons of Conventional Phonon Scattering and Excavation of Heikes’ Equation for Estimating Carrier Properties,” *Advanced Energy Materials* 11 (2021): 2101122, https://doi.org/10.1002/aenm.202101122.

56. A. Li, L. Wang, J. Li, and T. Mori, “Global Softening To Manipulate Sound Velocity For Reliable High-Performance MgAgSb Thermoelectrics,” *Energy & Environmental Science* 17 (2024): 8810–8819, https://doi.org/10.1039/D4EE03521F.

57. S. Lee, K. Esfarjani, T. Luo, J. Zhou, Z. Tian, and G. Chen, “Resonant Bonding Leads To Low Lattice Thermal Conductivity,” *Nature Communications* 5 (2014): 3525, https://doi.org/10.1038/ncomms4525.

58. M. T. Agne, R. Hanus, and G. J. Snyder, “Minimum Thermal Conductivity In The Context Of Diffuson-Mediated Thermal Transport,” *Energy & Environmental Science* 11 (2018): 609–616, https://doi.org/10.1039/C7EE03256K.

59. P. B. Allen, X. Du, L. Mihaly, and L. Forro, “Thermal Conductivity Of Insulating $Bi_2Sr_2YCu_2O_8$ and Superconducting $Bi_2Sr_2CaCu_2O_8$: Failure Of The Phonon-Gas Picture,” *Physical Review B* 49 (1994): 9073–9079, https://doi.org/10.1103/PhysRevB.49.9073.

60. L. Zheng, W. Li, S. Lin, J. Li, Z. Chen, and Y. Pei, “Interstitial Defects Improving Thermoelectric SnTe in Addition to Band Convergence,” *ACS Energy Letters* 2 (2017): 563–568, https://doi.org/10.1021/acsenergylett.6b00671.

61. M. J. Krogstad, S. Rosenkranz, J. M. Wozniak, et al., “Reciprocal Space Imaging Of Ionic Correlations In Intercalation Compounds,” *Nature Materials* 19 (2020): 63–68, https://doi.org/10.1038/s41563-019-0500-7.

62. R. Osborn and J. Wozniak, NeXpy; Github, https://github.com/nexpy/nexpy.

63. R. Osborn, M. Krogstad, and J. Wozniak, NXrefine; Github, https://github.com/nexpy/nxrefine.

64. G. Jennings, “Crystal Coordinate Transformation Workflow (CCTW); SourceForge,” (2019), https://sourceforge.net/projects/cctw/.

Supporting Information

Additional supporting information can be found online in the Supporting Information section.

Supporting File: adfm74755-sup-0001-SuppMat.docx.